Geophys. J. Int. (2002) **149,** 482–489

Constraints on the correlation of *P*- and *S*-wave velocity heterogeneity in the mantle from *P*, *PP*, *PPP* and *PKP*ab traveltimes

Jeroen Ritsema and Hendrik-Jan van Heijst

Seismological Laboratory 252-21, *California Institute of Technology, Pasadena, CA* 91125, *USA. E-mail: jeroen@gps.caltech.edu*

Accepted 2001 October 10. Received 2001 October 1; in original form 2001 April 9

SUMMARY

We investigate the correlation of large-scale *P*- and *S*-velocity heterogeneity in the mantle by determining how well 106,000 compressional *P*, *PP*, *PPP*, and *PKP*ab traveltimes can be explained by *S*-wave velocity model S20RTS (scaled using a depth dependent factor) and by a model in which the lateral *P*-velocity variations are different. We first assess the assumption that *P*-wave traveltimes can be explained by a model in which lateral *P*-velocity variations (δv_P) are identical to *S*-velocity variations (δv_S) in model S20RTS. For a given depth, we project δv_S from S20RTS into model S2P using a depth-dependent scaling factor $\mathcal{R}$ defined as: $\delta v_S = \mathcal{R}(z) \times \delta v_P$. We find, by grid search, that the highest reduction of data variance is obtained when $\mathcal{R}$ increases linearly from 1.25 at the surface to 3.0 at the core–mantle boundary. A comparison of *S*-wave ($+SS$) and *P*-wave ($+PP$) traveltimes for identical source–receiver pairs also indicates that $\mathcal{R}$ increases with depth. Significantly higher variance reduction is not obtained when $\mathcal{R}$ is parametrized with an additional degree of freedom. Therefore, the precise shape of $\mathcal{R}$ cannot be constrained by our data.

P- and *PP*-wave traveltime anomalies with respect to the scaled model S2P yield coherent geographic variations. This indicates that there are large-scale lateral *P*-velocity variations in the mantle that are different from those in model S2P. We estimate these variations by inverting *P*-wave traveltime anomalies with respect to model S2P for a degree 12 model of *P*-velocity heterogeneity. This model, $\mathrm{P12}^{\mathrm{s2p}}$, indicates where in the well-sampled mantle regions we need to modify model S2P to further improve the fit to the traveltime data. Anomalies in $\mathrm{P12}^{\mathrm{s2p}}$ exist throughout the mantle. It is, therefore, not obvious that compositional heterogeneity is prominent in the lower 1000 km of the mantle only, as suggested previously. Low *P*-wave velocities in the upper mantle beneath oceans are the strongest anomalies in $\mathrm{P12}^{\mathrm{s2p}}$ and explain better the delayed traveltimes of *PP*-wave phases with oceanic surface refection points. Lower mantle anomalies include high and low *P*-velocity structures beneath eastern Asia and North America, respectively. The high *P*-velocity anomaly in the lower mantle beneath the central Pacific is consistent with the assertion made by other researchers that large-scale lower mantle upwellings are not purely thermal in origin.

Key words: global tomography, mantle dynamics, *P*-wave and *S*-wave velocity.

1 INTRODUCTION

The steady increase in the quality of models of shear-velocity heterogeneity (e.g. Masters *et al.* 1996; Liu & Dziewonski 1996; Ritsema *et al.* 1999; Mégnin & Romanowicz 2000) and *P*-velocity heterogeneity (e.g. van der Hilst *et al.* 1997; Vasco & Johnson 1998; Bijwaard *et al.* 1998; Boschi & Dziewonski 1999) has led to detailed models of dynamic processes. These include models of slab descent into the lower mantle (e.g. Lithgow-Bertelloni & Richards 1998; Bunge & Grand 2000), the formation of broad thermo-chemical upwellings from the Core–Mantle Boundary (CMB) region (e.g. Gurnis *et al.* 2000; Tackley 2000), and compositional stratification in the deep mantle (e.g. Kellogg *et al.* 1999).

To large extent, these models rely on our ability to recognise the robust features common to *S*- and *P*-velocity models (e.g. Grand *et al.* 1997). However, comparing *S*- and *P*-velocity models is by no means straightforward. While *S*-velocity structure can be constrained with a variety of data types including free-oscillation spectra, surface-wave phase- and group-velocities, and body-wave traveltimes, it is more difficult to constrain *P*-velocity heterogeneity

in the mantle because fewer *P*-wave types are recorded and low-frequency seismic waves have limited sensitivity to *P*-velocity structure.

One approach is to constrain *S*- and *P*-velocity heterogeneity with the same accuracy by joint inversions (e.g. Vasco *et al.* 1994; Robertson & Woodhouse 1995, 1996; Su & Dziewonski 1997; Kennett *et al.* 1998; Masters *et al.* 2000), or analyses of the global variation of *S*-wave and *P*-wave traveltimes (e.g. Saltzer *et al.* 2001; Bolton & Masters 2001) for common source–receiver pairs. Here we take an alternative approach in which we verify explicitly the correlation of *S*- and *P*-velocity heterogeneity in the mantle. First, we assume that *P*-velocity heterogeneity is, except for a depth-dependent scaling factor $\mathcal{R}$, identical to large-scale *S*-velocity structure and that it is optimally resolved by *S*-wave tomography. We estimate $\mathcal{R}$ by grid-search. Subsequently, we determine whether *P*-wave traveltimes can be explained better when lateral variations of *P*-velocity in the scaled model are modified. The advantage of this approach is that we do not need to make data restrictions. Moreover, recent *S*-velocity models from various research groups compare extremely well at the long wavelengths (<degree 12) so that the analysis is not highly dependent on the choice of the *S* velocity model.

2 BODY-WAVE TRAVELTIME MEASUREMENTS BY WAVEFORM FITTING

We generate a set of traveltime anomalies by cross-correlating low-pass filtered (T > 16 s) broadband seismograms with normal-mode synthetics for the PREM seismic velocity structure and Harvard-CMT source parameters. The waveshape of a long-period body-wave is not strongly complicated by the earthquake rupture process, complex crustal reverberations and microseismic noise. Waveform fitting allows us to determine the traveltimes of first-arrivals (e.g. *P*, *S*, *SKS*) as well as other major *P*-wave ($P_{\rm diff}$, *PP*, *PPP*, *PKP*ab) and *S*-wave ($S_{\rm diff}$, *SS*, *SSS*, *ScS*, ScS_2, *SKKS*) phases with the same accuracy.

We apply several criteria to identify unreliable measurements. For example, we discard seismograms with high noise levels before the first-arrival and high-amplitude coda. We do not measure the traveltime of a body-wave that arrives within 40 s of another major body-wave phase. We define two quantities of the similarity between recorded ($d(t)$) and synthetic ($s(t)$) waveforms. The first quantity is the least-squares misfit between recorded and synthetic waveforms within a window w:

$$\mathrm{F}_1 = \frac{\int_w [d(t) - s(\tau_m - t)]^2\, dt}{\int_w d(t)^2\, dt}. \tag{1}$$

Here, τ_m is the time-shift of the synthetic (i.e. the traveltime delay) at which the cross-correlation function has a maximum. We use a 40-s long cross-correlation window centred about the predicted arrival time. The second quantity is defined as:

$$\mathrm{F}_2 = \frac{\min(A_1, A_2)}{\max(A_1, A_2)}, \tag{2}$$

where A_1 and A_2 are amplitude factors that minimize

$$\int_w [d(t) - A_1 s(\tau_m - t)]^2\, dt \tag{3}$$

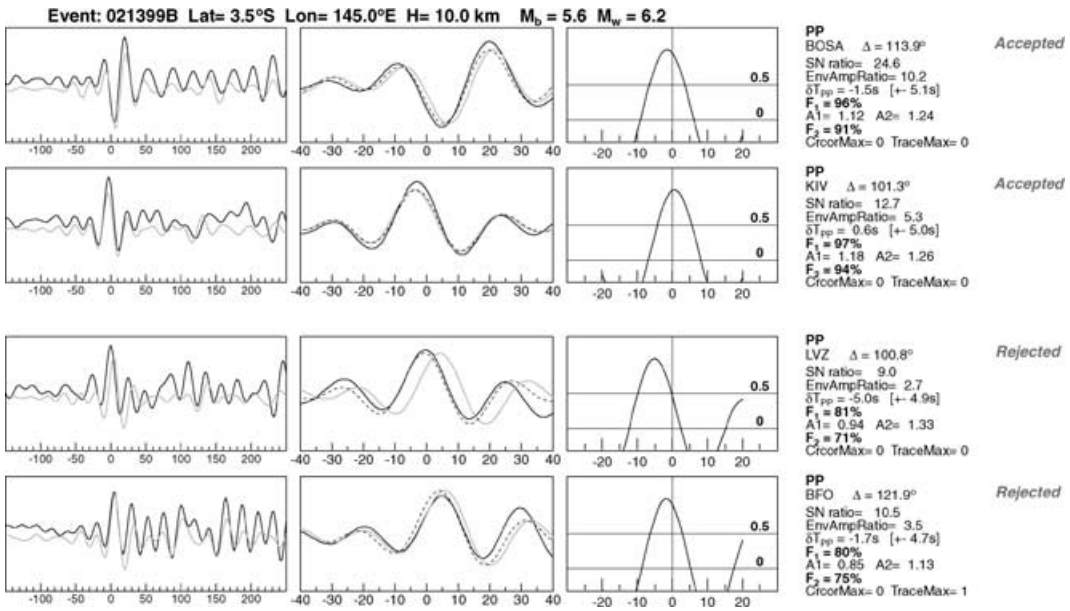

Figure 1. Examples of *PP*-wave traveltime measurements for event 021399B recorded at global stations BOSA, KIV, LVZ, and BFO. The left panel compares seismograms (dark line) and PREM synthetics (grey line) about the predicted *PP*-wave arrival for a 400 s long window, while the middle panel shows the PREM fit as well as the best-fitting synthetic (dashed line) after a time shift δT_{PP} has been applied. The right column shows the cross-correlation function. The variables provided on the right are the criteria used to consider whether a measurement is reliable or not. The *PP*-wave traveltime measurements for stations BOSA and KIV are regarded as 'acceptable' because F_1 and F_2 are higher than 0.8, the *PP*-wave is simple and well above noise level, and the cross-correlation function does not have a secondary maximum. The *PP*-wave traveltime measurement for station LVZ is rejected because F_2 is relatively low (71 per cent) in part due to the waveform mismatch at the onset of *PP*. The measurement for station BFO is rejected (TraceMax = 1) due to the large-amplitude coda following *PP*.

Table 1. Number of traveltime measurements.

Seismic phase	# of traveltime measurements
P (+*pP*, *sP*)	61,492
PP	40,487
PPP	4,005
*PKP*ab	253
SP + *SKP* + *ScP*	1,004
Total	106,237

and

$$\int_w \left[A_2^{-1} d(t) - s(\tau_m - t)\right]^2 dt. \quad (4)$$

When the wave shapes of $s(t)$ and $d(t)$ are identical, A_1 is equal to A_2 and represents the ratio between the maximum amplitude of $d(t)$ and $s(\tau_m - t)$. When $s(\tau_m - t)$ and $d(t)$ have dissimilar wave shapes, A_1 is not equal to A_2 and, hence, F_2 is less than 1. By experimentation we found that the observed and synthetic waveforms match well in the entire cross-correlation window when we require that F_1 and F_2 are greater than 0.8 (Fig. 1).

On average, we retain about 60 per cent of the number of traveltime measurements compared to the number we would obtain had we inspected the data interactively (Ritsema & van Heijst 1999). At the expense of discarding nearly half of what is possibly good data, we enable ourselves to process large data volumes in a routine manner. While making measurements by hand for an earthquake recorded at more than 100 stations (this is typically the case for post-1998 earthquakes) takes about 30 min, we can automatically process such a data set in less than 40 s. Moreover, automatic processing yields quantitative reliability measurements via F_1 and F_2 and it enables us to reanalyse the data with different processing parameters with little effort.

So far, we have measured about 106 000 *P*-wave traveltimes (Table 1) and 120 000 *S*-wave traveltimes for about 4000 earthquakes (1980–2000) listed in the Harvard-CMT catalog with a body-wave magnitude larger than 5.9. Seismograms were recorded at stations from the global IRIS and GEOSCOPE networks, permanent regional networks (e.g. CNSN, USNSN, GRSN), and PASSCAL deployments (e.g. Tibet, Banjo, BSLP, Tanzania). Prior to analysis, we correct the traveltime anomalies for the effects of Earth's ellipticity and variations of crustal structure using model CRUST5.1 (Mooney *et al.* 1998). In addition, we relocate earthquakes by minimizing the variance of traveltime anomalies (with a L-1 norm) using model S12 (discussed below) under the assumption that lateral *P*-velocity variations in the mantle are half as large as *S*-velocity variations.

3 THE SCALING BETWEEN *S*- AND *P*-VELOCITY HETEROGENEITY IN THE MANTLE

We estimate first how well our traveltime data can be explained by a model in which, at a given depth, lateral *P*-velocity variations are identical to those in the global *S*-velocity model S20RTS (Ritsema *et al.* 1999), truncated to degree 12. We call this model from here on S12. We project the heterogeneity of S12 into the *P*-velocity model S2P using a depth-dependent scaling factor $\mathcal{R}$:

$$\delta v_S = \mathcal{R} \times \delta v_P. \quad (5)$$

By grid-search, we estimate $\mathcal{R}$ that renders the highest variance reduction of the traveltime data. To limit the number of parameters that describe $\mathcal{R}$, we begin with the assumption that $\mathcal{R}$ varies linearly with depth and parametrize it by its value at the surface ($\mathcal{R}_0$) and its value at the CMB ($\mathcal{R}_{2891}$). Theoretical traveltimes are computed by ray tracing through models for which $\mathcal{R}_0$ and $\mathcal{R}_{2891}$ vary between 1.0 and 4.5. Table 2 indicates the fit to *P*, *PP*, and *PPP* separately for several models. The 'total' variance reduction is determined by weighing *P*-wave, *PP*-wave, and *PPP*-wave traveltime anomalies equally.

Fig. 2(a) shows how total variance reduction varies as a function of $\mathcal{R}_0$ and $\mathcal{R}_{2891}$. Model S2P for which $\mathcal{R}_0 = 1.25$ and $\mathcal{R}_{2891} = 3.0$ explains the data best. Models for which $\mathcal{R}$ decreases with depth render a poor fit of especially *PP*-wave and *PPP*-wave traveltimes. Model S2P for which $\mathcal{R}_0 = 1.25$ and $\mathcal{R}_{2891} = 3.0$ explains the data best. Total variance reduction for model S2P (61 per cent) is about 3 per cent higher than for models in which $\mathcal{R}$ is constant throughout the mantle. This is a significant difference considering that we are analysing over 100 000 traveltimes and that we use only two parameters to describe model S2P. However, our preference for model S2P over models in which $\mathcal{R}$ is constant throughout the mantle stems also from a comparison of *S*-wave and *P*-wave traveltime anomalies (Fig. 3).

In Fig. 3 we plot *SS*-wave traveltime anomalies against *PP*-wave traveltime anomalies and *S*-wave anomalies against *P*-wave anomalies. We consider only those recordings which yield reliable traveltime estimates for both *S* and *P* or *SS* and *PP*. The *SS*-wave and *PP*-wave anomalies are selected for source–receiver distances between 60° and 90°. Within this distance range, *SS*-wave and *PP*-wave propagation is confined to the upper half of the mantle. The *S*-wave and *P*-wave traveltimes are selected for source–receiver distances larger than 103° when *S*-waves and *P*-waves propagate a significant distance along the CMB. The best-fitting line through the *S*-wave and *P*-wave traveltime anomalies is significantly steeper than the best-fitting line through the *SS*-wave and *PP*-wave data. This indicates

Table 2. Variance reduction of *P* traveltime data.

Model	Fit to *P* (per cent)	Fit to *PP* (per cent)	Fit to *PPP* (per cent)	Total (per cent)
Earthquake relocation	41	24	3	33
$\mathcal{R}$ *is constant*				
1: $\mathcal{R} = 1.25$	60	58	41	58
2: $\mathcal{R} = 2.00$	63	54	35	58
3: $\mathcal{R} = 3.00$	63	48	28	55
$\mathcal{R}$ *varies linearly*				
4: $\mathcal{R}_0 = 3.00$ $\mathcal{R}_{2891} = 1.25$	61	49	30	55
5: $\mathcal{R}_0 = 1.25$ $\mathcal{R}_{2891} = 3.00$	63	59	42	61
Degree-12 *inversion*				
$P12^{s2p}$	68	74	68	70

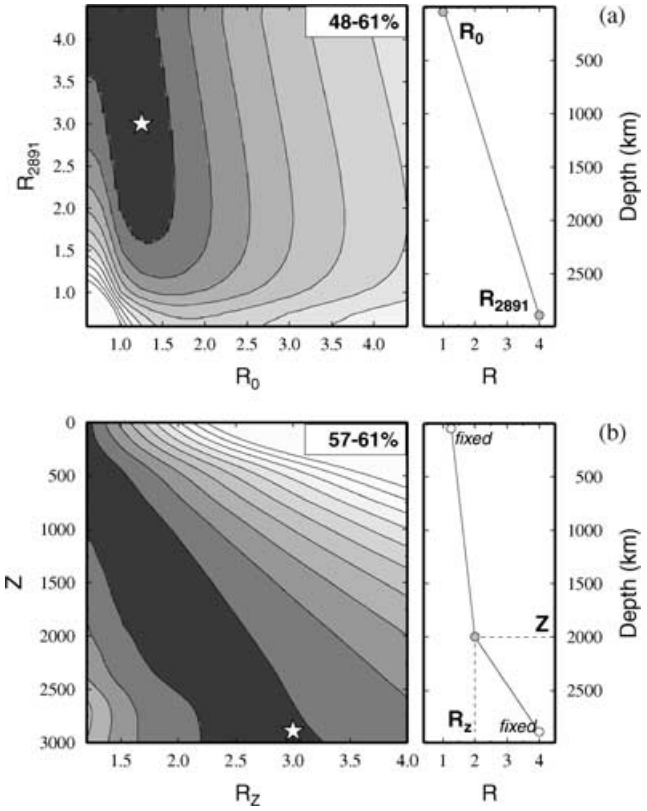

Figure 2. Total variance reduction of *P*, *PP*, and *PPP* traveltime anomalies (weighed equally) for *P*-velocity models constructed by scaling model S20RTS (Ritsema *et al.* 1999) with a depth-dependent factor $\mathcal{R}$. (a) shows the fit for models in which $\mathcal{R}$ from the surface (*x*-axis) to the CMB (*y*-axis) varies linearly with depth. $\mathcal{R}$ that renders a best fit to the data (star) has a value of 1.25 at the surface and 3.0 at the CMB. (b) shows the fit for models in which $\mathcal{R}$ is constrained to be 1.25 at the surface and 4.0 at the CMB, while it varies linearly with depth changing slope at depth Z. The fit is plotted as a function of Z and the value of $\mathcal{R}$ at Z. The fit is progressively better in regions shaded darker. The range in data fit is shown in the upper-right corner. The models shown on the right schematically show the structure of $\mathcal{R}$ that we are investigating.

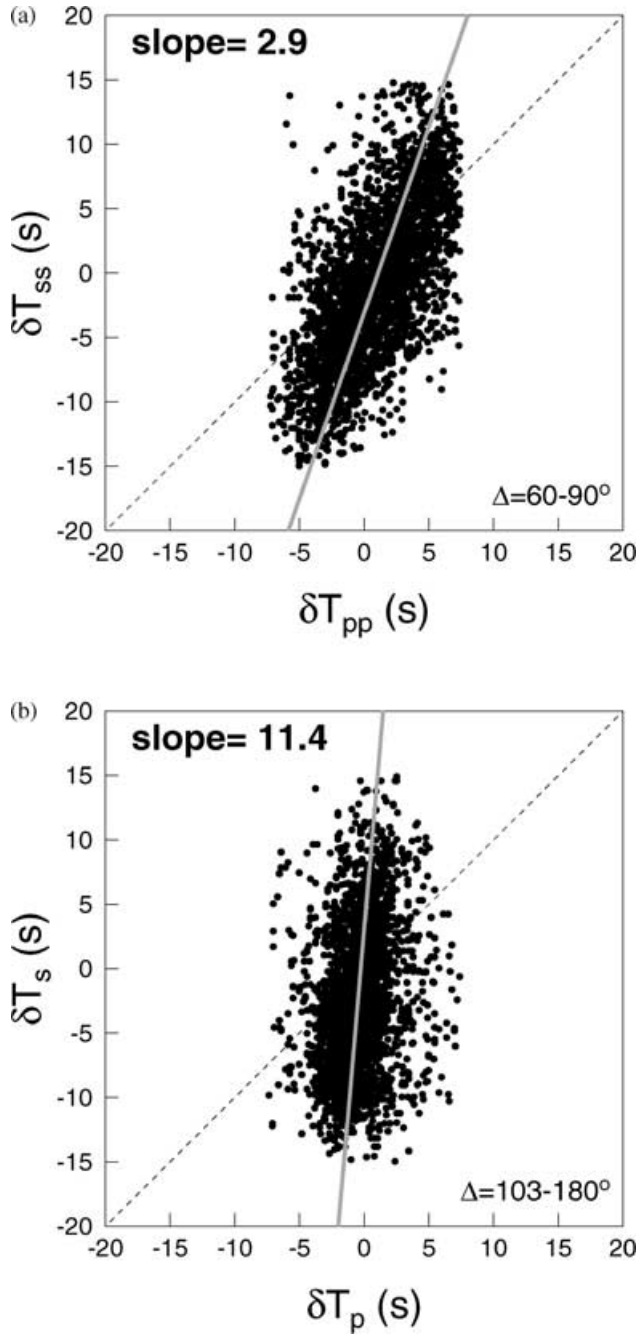

Figure 3. Comparison of traveltime anomalies of (a) the phases *SS* and *PP* and (b) *S* and *P* recorded at the same station. The *PP*-wave and *SS*-wave data are restricted to recordings from stations at an epicentral distance between 60° and 90°. Within this epicentral distance range, *PP*-waves and *SS*-waves propagate along similar paths within the upper half of the mantle. Traveltimes of *S*-waves and *P*-waves are recorded at seismic stations at epicentral distances larger than 103°, for which *S*-waves and *P*-waves diffract along the CMB. The significantly larger $\frac{\delta T_S}{\delta T_P}$ ratio compared to $\frac{\delta T_{SS}}{\delta T_{PP}}$ indicates that $\mathcal{R}$ in the lower mantle is larger than $\mathcal{R}$ in the upper mantle.

that the effect of seismic velocity heterogeneity on *S*-wave traveltimes, compared to its effect on *P*-wave traveltimes, is strongest for paths that sample the deepest parts of the mantle. In other words, it indicates that $\mathcal{R}$ increases with depth.

Fig. 2(b) demonstrates that we do not improve the fit at all when we invoke a depth-dependent scaling factor $\mathcal{R}$ described by an additional degree of freedom. We show a contour plot of total variance reduction for models with $\mathcal{R}_0 = 1.25$ and $\mathcal{R}_{2891} = 4.0$. In the mantle, $\mathcal{R}$ varies linearly with depth and may change its slope at depth *Z*. Variance reduction of the traveltime data is shown as a function of *Z*, and the value of $\mathcal{R}$ at *Z*. The maximum misfit reduction is only 0.1 per cent higher than the misfit reduction obtained for model S2P, independent on the values we have chosen for $\mathcal{R}_0$ and $\mathcal{R}_{2891}$.

4 DE-CORRELATION OF *P*- AND *S*-VELOCITY HETEROGENEITY

The fact that model S2P renders 61 per cent variance reduction demonstrates that, to a large extent, *P* and *S*-wave velocity heterogeneity in the mantle are correlated. However, coherent geographic variations in *P*-wave and *PP*-wave traveltimes, when they are referenced to model S2P, persist (Fig. 4). For example, traveltimes of *PP*-waves with respect to model S2P are systematically low when they have oceanic surface reflection points while *P*-waves propagate slowly when they diffract around the core beneath eastern Asia and North America, respectively. The presence of these anomalies indicate that there are *P*-velocity variations in the mantle that are different than in the scaled model S2P. In order to constrain where

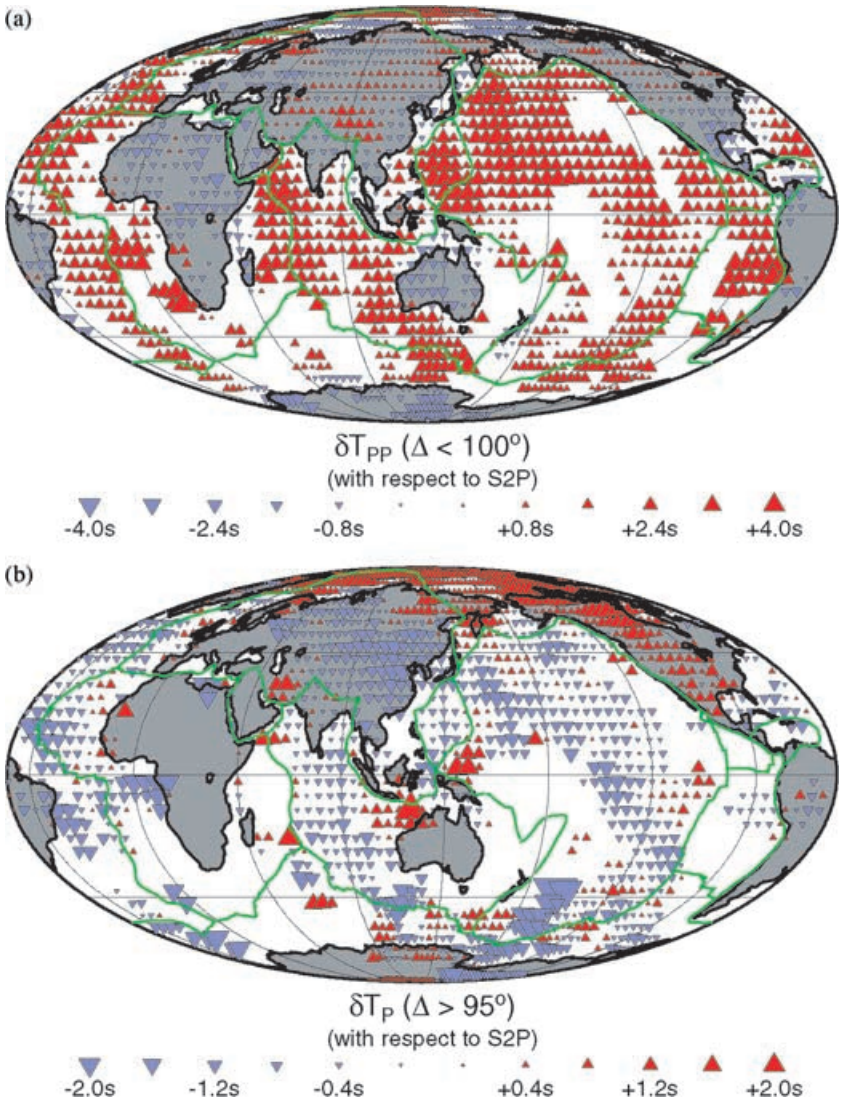

Figure 4. Traveltime anomalies of (a) *PP*, plotted at the surface reflection points, for epicentral distances smaller than 100° and (b) *P*, plotted at the turning points, for epicentral distances larger than 95° with respect to model S2P after averaging at least 10 measurements within a cap that is 5° wide.

in the mantle these anomalies reside, we apply a tomographic inversion to 'residual' traveltime data. The residual traveltimes (δT^{s2p}) are the *P*-wave traveltimes now referenced to model S2P. The ensuing model, $P12^{s2p}$, presents *P*-velocities anomalies with respect to S2P. That is, model $P12^{s2p}$ shows how the best-fitting scaled model needs to be modified in order to explain the traveltime data best.

We can only expect to observe anomalies in $P12^{s2p}$ in well-sampled regions of the mantle (Fig. 5). We anticipate poor vertical resolution in the upper mantle because teleseismic body-waves sample this regions predominantly in near-vertical direction while anomalies in $P12^{s2p}$ in the deep mantle are most robust in the central-northern Pacific, where data coverage is best.

Since seismic velocity variations in model S2P differ from those in PREM by only several percent, we simplify the inversion of δT^{s2p} by assuming that *P*-wave traveltimes accumulate along *P*-wave ray paths for the 1-D PREM velocity model (S^0):

$$\delta T^{s2p} = -\int_{S^0} \frac{\delta V(\mathbf{r})}{V^2_{s2p}(\mathbf{r})}\, ds. \qquad (6)$$

In matrix form, this relationship can be written as

$$\mathbf{Am} = \mathbf{d}, \qquad (7)$$

where **m** and **d** represent the model vector and the data vector δT^{s2p}, respectively. We use spherical harmonics (up to order and degree 12) and 21 spline functions to describe lateral and vertical variations in $P12^{s2p}$. We solve eq. (7) by least-squares inversion. We apply model norm damping to minimize the amplitude of *P*-velocity variations in poorly sampled mantle regions. Model $P12^{s2p}$ provides 70 per cent variance reduction (see Table 1).

Fig. 6 shows model $P12^{S2p}$ at a depth of 600 km, 1400 km, 2000 km, 2650 km, and 2850 km. We emphasize that model $P12^{s2p}$ does not represent *P* velocity heterogeneity with respect to a standard 1-D model as is typical in *P*-wave traveltime tomography. Rather, it indicates where in the mantle the *P*-velocity is higher or lower than expected for a scaled *S*-velocity model (S2P in our case). Several outstanding anomalies in $P12^{s2p}$ can be associated to the traveltime anomalies of Fig. 4. The low *P*-velocities in the upper mantle beneath oceans are related to delayed *PP*-waves which reflect off the ocean floor. Due to the low vertical resolution of model $P12^{s2p}$ in the uppermost mantle—a characteristic common to models based

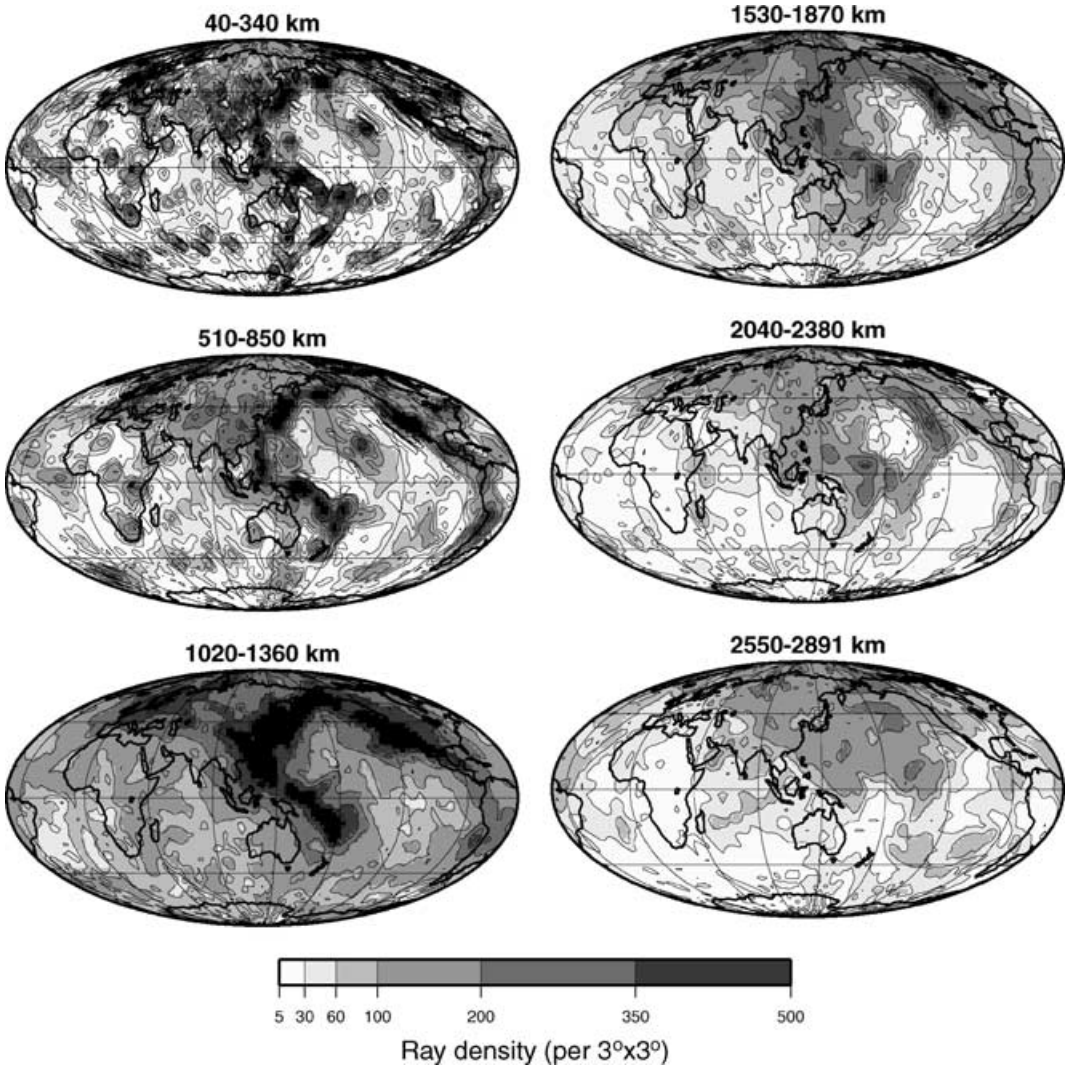

Figure 5. Ray density (per $3^\circ \times 3^\circ$) of *P*, *PP*, *PPP*, and *PKP*ab phases in 340 km thick mantle layers. Note that *P*-wave sampling of the mantle is heterogeneous. *P*-waves sample the upper most mantle (layer '40–340 km') only beneath earthquakes, seismic stations, and surface reflections points of *PP*-waves and *PPP*-waves. Core–Mantle Boundary sampling (layer '2550–2891 km') is best in the northern Pacific, North America, and eastern Asia. A high number of long-range ($\Delta > 80^\circ$) *P*- and diffracted *P*-waves from between earthquakes in the western Pacific and stations in North America and Europe traverse these regions.

solely on teleseismic body-wave traveltimes—this anomaly is likely 'smeared' throughout the upper mantle. Therefore, we suspect that these anomalies are confined to the uppermost 200–300 km of the mantle and that they have a much larger amplitude than suggested by model $P12^{s2p}$. At the CMB, we observe a high velocity anomaly beneath eastern Asia and a low velocity anomaly beneath North America, which, according to Fig. 4, are related to diffracted *P*-waves which propagate from western Pacific earthquakes to stations in Europe and from earthquakes in the western Pacific to stations North America, respectively. Note also the high velocity anomaly beneath the central Pacific several hundred kilometres above the CMB. This anomaly is related to fast *P*-wave propagation between southwestern Pacific earthquakes and stations in western North America, turning several hundred kilometers above the CMB. At 1400 km and 2000 km traveltime anomalies cannot be easily related to surface geologic structures or large anomalies in model S12. However, the excellent sampling of the mid mantle by *P*-waves (Fig. 5) suggest that these anomalies are well resolved.

To facilitate a comparison with other *P*-velocity models which are constructed with respect to 1-D reference models we show in the third column of Fig. 6 how model $P12^{s2p}$ relates to a model of *P*-wave velocity anomalies with respect to PREM. This model, $P12^{prem}$, can be constructed by simply adding model $P12^{s2p}$ to S2P:

$$P12^{prem} = S2P + P12^{s2p}. \quad (8)$$

Model $P12^{prem}$ should be interpreted cautiously because it inherits velocity anomalies from model S12 that are not necessarily constrained by the *P*-wave traveltime data such as, for example, the strong western-Pacific subduction zone anomaly at 600 km depth. Moreover, the poor vertical resolution is likely the reason why low *P*-wave velocity anomalies in the upper mantle beneath oceans are apparent in the transition zone, as discussed above. The comparison between $P12^{prem}$ and S12 is meaningful mostly for depths larger than about 1500 km, where both *P*- and *S*-velocity heterogeneity are primarily resolved by traveltime data. Model $P12^{prem}$ emphasizes the absence of high *P*-wave velocity anomalies in the lowermost mantle beneath North America, and the fact that the high velocity anomaly beneath eastern Asia is much stronger than predicted on the basis of scaled models.

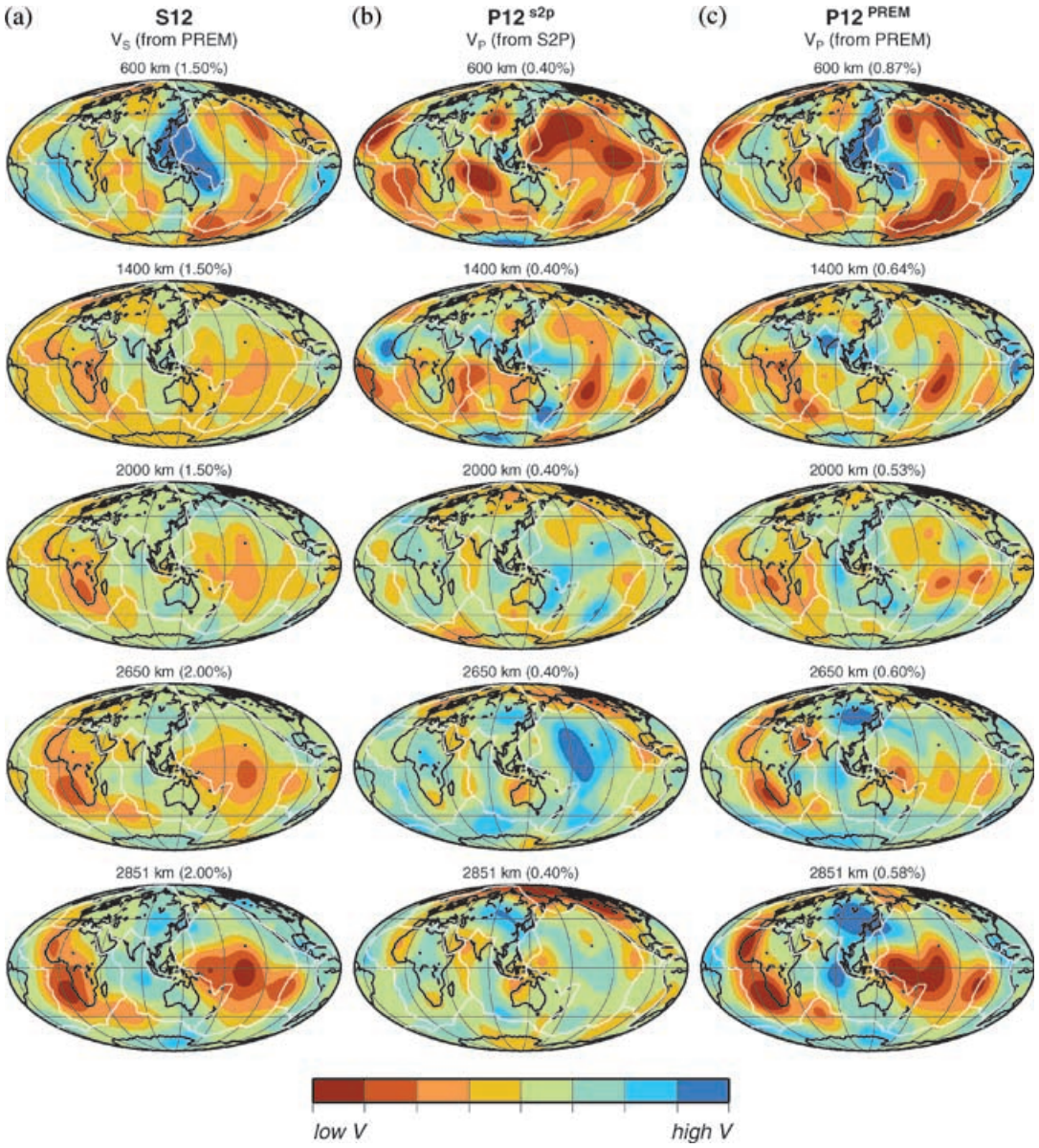

Figure 6. Variation of (a) *S*-velocity with respect to PREM for model S12, (b) *P*-velocity with respect to model S2P and (c) *P*-velocity with respect to PREM at a depth of 150 km, 600 km, 1400 km, 2000 km, 2650 km and 2851 km. The velocity in regions shaded red (blue) is lower (higher) than in the reference model for that depth, with a range that is indicated in brackets. The maximum amplitude of the scale used to plot $P12^{prem}$ is smaller than that of model S12 by a factor $\mathcal{R}$.

5 DISCUSSION AND CONCLUSIONS

A total of 106 000 measurements of *P*, *PP*, *PPP*, and *PKP*ab traveltimes indicate that *P*- and *S*-velocity heterogeneity are well correlated. We find that model S2P, in which the ratio between shear velocity and *P* velocity heterogeneity ($\mathcal{R} = \frac{\delta v_S}{\delta v_P}$) increases linearly from 1.25 at the surface to 3.0 at the CMB, provides highest data variance reduction of 61 per cent. Due to the scatter in the data, we cannot precisely constrain the slope of $\mathcal{R}$, nor do we achieve higher variance reductions for structures of $\mathcal{R}$ that are more complex. Our inference that $\mathcal{R}$ increases with depth agrees with the traveltime studies of Robertson & Woodhouse (1995) and Bolton & Masters (2001) and the free-oscillation study of Ishii & Tromp (2001). It does not agree with the traveltime study of Saltzer *et al.* (2001) who suggest that $\mathcal{R}$ decreases with depth below a depth of 2000 km. The discrepancy is possibly due to the fact that Saltzer *et al.* (2001) restricted their data analysis to *P*-wave and *S*-wave traveltime anomalies smaller than 7.5 s and opted not to analyse ISC *SS*-wave and *PP*-wave traveltimes due to their low quality.

When we invert traveltime anomalies with respect to S2P for the degree-12 model $P12^{s2p}$ of *P*-velocity heterogeneity in the mantle the data variance reduction growths to 71 per cent. Low upper-mantle *P*-velocities beneath oceans can readily be related to relatively slow *PP*-waves that reflect off the ocean floor. This anomaly is strongest at a depth of 800 km, but due to the poor vertical resolution in the upper mantle we suspect that this anomaly resides with higher amplitude in the upper 200–300 km of the mantle. Outstanding deep mantle anomalies include the low *P*-velocities in the CMB region beneath North America and the Arctic, low velocities beneath the central Pacific and high velocities beneath eastern Asia.

P-velocity anomalies with respect to model S2P correspond in shape (but not in magnitude) to bulk-wave speed anomalies with

respect to PREM. Thus, the relatively high *P*-velocity anomaly (with respect to *S*2*P*) beneath the Pacific relates to a high bulk-wave speed anomaly with respect to PREM. The anticorrelation between *S*-velocity and bulk-wave speed anomalies in lower mantle regions associated with large-scale mantle upwelling has been observed previously (e.g. Su & Dziewonski 1997; Masters *et al.* 2000). The anticorrelation between *S*-velocity and bulk-wave speed is not obvious in the lower mantle beneath eastern Asia, a region where downwellings characterize mantle flow (e.g. Lithgow-Bertelloni & Richards 1998; van der Voo *et al.* 1999).

ACKNOWLEDGMENTS

Data have been provided by the IRIS/DMC in Seattle, WA. All figures have been produced using the GMT software of Wessel & Smith (1995). We thank Steve Ward and the anonymous reviewers for helpful comments. This research was funded by NSF grant EAR-0106666. This is contribution number 8802 of the Division of Geological and Planetary Sciences of the California Institute of Technology.

REFERENCES

Bijwaard, H., Spakman, W. & Engdahl, E.R., 1998. Closing the gap between regional and global travel time tomography, *J. geophys. Res.,* **103,** 30 055–30 078.

Bolton, H. & Masters, G., 2001. Travel time of P and S from the global digital seismic networks: Implications for the relative variation of P and S velocity in the mantle, *J. geophys. Res.,* **106,** 13 527–13 540.

Boschi, L. & Dziewonski, A.M., 1999. High and low resolution images of the Earth's mantle—Implications of different approaches to tomographic modeling, *J. geophys. Res.,* **104,** 25 567–25 594.

Bunge, H.P. & Grand, S.P., 2000. Mesozoic plate-motion history below the northeast Pacific from seismic images of the subducted Farallon slab, *Nature,* **405,** 337–340.

Grand, S.P., van der Hilst, R.D. & Widiyantoro, S., 1997. Global seismic tomography: a snapshot of convection in the Earth, *GSA Today,* **7,** 1–7.

Gurnis, M., Mitrovica, J.X., Ritsema, J. & Heijst, H.J.V., 2000. Constraining mantle density structure using geological evidence of surface uplift rates: The case of the African Superplume, *Geochem. Geophys. Geosys.,* **1**.

Ishii, M. & Tromp, J., 2001. Even-degree lateral variations in Earth mantle constrained by free oscillations and the free-air gravity anomaly, *Geophys. J. Int.,* **145,** 77–96.

Kellogg, L.H., Hager, B.H. & van der Hilst, R.D., 1999. Compositional stratification in the deep mantle, *Science,* **283,** 1881–1884.

Kennett, B.L.N., Widiyantoro, S. & van der Hilst, R.D., 1998. Joint seismic tomography for bulk sound and shear wave speed in the Earth's mantle, *J. geophys. Res.,* **103,** 12 469–12 493.

Lithgow-Bertelloni, C. & Richards, M.A., 1998. The dynamics of Cenozoic and Mesozoic plate motions, *Rev. Geophys.,* **36,** 27–78.

Liu, X.F. & Dziewonski, A.M., 1996. Global analysis of shear wave velocity anomalies in the lowermost mantle, in *The Core-Mantle Boundary Region,* Vol. 28, pp. 21–36, Geodynamics Series, American Geophysical Union, Washington DC.

Masters, G., Johnson, S., Laske, G. & Bolton, H., 1996. A shear velocity model of the mantle, *Phil. Trans. R. Soc. Lond.,* A., **354,** 1385–1411.

Masters, G., Laske, G., Bolton, H. & Dziewonski, A., 2000. The relative behavior of shear velocity, bulk sound speed, and compressional velocity in the mantle: Implications for chemical and thermal structure, in *Earth's Deep Interior: Mineral Physics and Tomography from the Atomic to the Global Scale,* Vol. 117, pp. 63–87, Geophysical Monograph American Geophysical Union, Washington DC.

Mégnin, C. & Romanowicz, B., 2000. The three-dimensional shear velocity structure of the mantle from the inversion of body, surface and higher-mode waveforms, *Geophys. J. Int.,* **143,** 709–728.

Mooney, W.D., Laske, G. & Masters, G., 1998. CRUST5.1: A global crustal model at $5^\circ \times 5^\circ$, *J. geophys. Res.,* **103,** 727–747.

Ritsema, J. & van Heijst, H.J., 1999. Introducing new body wave phases in global tomography, *EOS, Trans. Am. geophys. Un.,* S221.

Ritsema, J., van Heijst, H.J. & Woodhouse, J.H., 1999. Complex shear velocity structure imaged beneath Africa and Iceland, *Science,* **286,** 1925–1928.

Robertson, G.S. & Woodhouse, J.H., 1995. Evidence for proportionality of P and S heterogeneity in the lower mantle, *Geophys. J. Int.,* **123,** 85–116.

Robertson, G.S. & Woodhouse, J.H., 1996. Ratio of relative S-to-P-velocity heterogeneity in the lower mantle, *J. geophys. Res.-Solid Earth,* **101,** 20 041–20 052.

Saltzer, R., van der Hilst, R.D. & Karason, H., 2001. Comparing P and S wave heterogeneity in the mantle, *Geophys. Res. Lett.,* **28,** 1335–1338.

Su, W.J. & Dziewonski, A.M., 1997. Simultaneous inversion for 3-d variations in shear and bulk velocity in the mantle, *Phys. Earth planet. Inter.,* **100,** 135–156.

Tackley, P., 2000. Mantle convection and plate tectonics: Toward an integrated physical and chemical theory, *Science,* **288,** 2002–2007.

van der Hilst, R.D., Widiyantoro, S. & Engdahl, E.R., 1997. Evidence for deep mantle circulation from global tomography, *Nature,* **386,** 578–584.

van der Voo, R., Spakman, W. & Bijwaard, H., 1999. Mosozoic subducted slabs under Siberia, *Nature,* **397,** 246–249.

Vasco, D.W. & Johnson, L.R., 1998. Whole earth structure estimated from seismic travel times, *J. geophys. Res.,* **103,** 2633–2671.

Vasco, D.W., Johnson, L.R., Pulliam, R.J. & Earle, P.S., 1994. Robust inversion of IASP91 travel time residuals for mantle P and S velocity structure, earthquake mislocations, and station corrections, *J. geophys. Res.,* **99,** 13 727–13 755.

Wessel, P. & Smith, W.H.F., 1995. New version of the generic mapping tools released, *EOS, Trans. Am. geophys. Un.,* **76,** 329.